Journal of Nuclear Materials 390–391 (2009) 959–962

Contents lists available at ScienceDirect

Journal of Nuclear Materials

journal homepage: www.elsevier.com/locate/jnucmat

# Estimated RF sheath power fluxes on ITER plasma facing components

L. Colas [a,*], D. Milanesio [b], E. Faudot [c], M. Goniche [a], A. Loarte [d]

[a] *CEA, IRFM, F-13108 Saint-Paul-lez-Durance, France*
[b] *Dipartimento di Elettronica, Politecnico di Torino, 10129 Torino, Italy*
[c] *LPMIA, UMR 7040 CNRS, BP 239, F-54506 Vandœuvre cedex, France*
[d] *ITER Organization, Fusion Science and Technology Department Cadarache – Building 523, 13108 St. Paul-lez-Durance, France*

ARTICLE INFO

*PACS:*
52.30.−q
52.35.Mw
52.40.Fd
52.40.Kh
52.50.Qt

ABSTRACT

Using numerical simulation, a first estimate is made of power fluxes caused by radio-frequency sheaths on plasma facing components surrounding the ITER Ion Cyclotron Range of Frequencies wave launcher. Three toroidal strap phasings were considered, and four plasma scenarios covering a broad range of Scrape-Off Layer densities. Parallel heat fluxes up to ~16 MW/m$^2$ are obtained, localized in poloidal peaks whose radial extension (initially 4–35 mm) increases when nearby flux tubes are coupled by exchanging RF currents. Quantitative results strongly depend on the local density, both *via* the unperturbed input profiles and *via* subsequent RF-induced modifications by $E \times B_0$ convection. Sources of uncertainty and aspects requiring further validation are identified.

## 1. Motivations, background and methodology

On several magnetic fusion devices, during additional heating of the plasma with waves in the Ion Cyclotron Range of Frequencies (ICRF), specific localized heat loads have been measured at extremities of open flux tubes around powered wave launchers [1–5]. They are generally attributed to radio-frequency (RF) sheath rectification [6]. To design the ITER ICRF antenna and neighbouring Plasma Facing Components (PFCs), an estimate of the RF specific heat loads (both magnitude and distribution) was undertaken, for a realistic geometry of the ITER antenna front face and for an adequate range of Scrape-Off Layer (SOL) plasma conditions.

The estimate follows a methodology similar to those implemented to interpret TFTR [7] and Tore Supra [3] results, with however more self-consistency and a predictive approach. The three-dimensional (3D) distribution of RF near fields $E_{//\mathrm{RF}}$ in front of the ITER antenna was provided by the antenna code TOPICA [8], in absence of sheaths but accounting self-consistently for the plasma in the full-wave solver FELICE [9], contrary to earlier studies. From the RF fields the SEM code [10] was used to estimate a DC sheath voltage, and CELLS module [3] to evaluate RF-induced DC density modifications. Estimation was made delicate by our poor knowledge both of the ITER far SOL and of detailed sheath rectification processes. Uncertainty on input parameters was circumvented by considering four plasma scenarios, covering a broad range of far SOL density profiles. In SEM code each open magnetic flux tube around the ICRF launcher was treated as a symmetric double Langmuir probe connected to a source of oscillating potential $V_{\mathrm{RF}} = \int_L \mathbf{E}_{//\mathrm{RF}}.\mathbf{dl}$. Contrary to [6] nearby flux tubes were coupled by self-consistent transverse exchanges of RF currents via the plasma non-collisional RF conductivity. Due to the non-linear $I$–$V$ sheath characteristic, the RF solicitation $V_{\mathrm{RF}}$ enhances the DC sheath potential $V_{\mathrm{DC}}$ on each field line. Differential DC biasing of adjacent flux tubes drives $E \times B_0$ plasma convection, which re-distributes the local density [11]. The heat flux at field line ends was finally taken as the Bohm flux times the DC potential.

The paper details this simulation process, stresses at each step the physical implications of the underlying mechanisms, identifies sources of uncertainty and aspects requiring further experimental validation.

## 2. Input parameters: unperturbed profiles, antenna

'Near field' RF sheaths develop over a few centimetres in front of ICRF antennas. Four cases of ITER far SOL profiles were considered in Fig. 1, corresponding to ITER scenarios 2 and 4 in the central plasma [12]. For the first four centimetres in the SOL, density profiles were calculated by B2-Eirene [13]. Beyond, two extrapolations were performed for each scenario. Parallel particle losses were balanced by an outward convective flux $nv_{\mathrm{SOL}}$, with radial velocities $v_{\mathrm{SOL}}$ within the experimentally determined range [20;100] ms$^{-1}$ [14], leading to short and long SOLs. The temperature profiles were assumed flat consistent with typical experimental profiles [14]. The plasma parameters extrapolated at antenna mouth are summarized in Table 1. In particular (unperturbed) densities $n_{\mathrm{ant}}$ at the antenna mouth cover more than two orders of magnitude.

---

* Corresponding author.
*E-mail address:* laurent.colas@cea.fr (L. Colas).

0022-3115/$ - see front matter © 2009 Elsevier B.V. All rights reserved.
doi:10.1016/j.jnucmat.2009.01.248

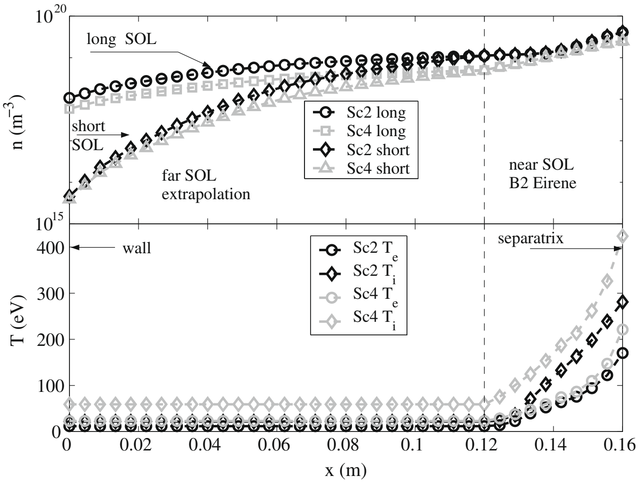

**Fig. 1.** Input density and temperature profiles in ITER mid-plane, versus radial distance to the wall, for the four scenari envisaged.

The simulated ICRF launcher ('external matching design', April 2007) consisted of a 6 × 4 phased array of radiating straps embedded in individual boxes, each partially closed by three horizontal Faraday screen bars. The antenna front face was flattened consistently with the SLAB geometry of the simulation, and recessed in a metallic wall, i.e., it behaves electrically as if the plug was grounded to the port on its front side. Three toroidal strap phasings were envisaged: [0 0 π π], [0 π π 0] and [0 π 0 π]. The poloidal strap phasing was [0 0 0 π π π]. All TOPICA simulations were conducted at RF frequency 53 MHz, with magnetic field $B_0 = 3.9$ T near the antenna.

## 3. Topologies of RF fields, RF potentials and DC potentials

Fig. 2 shows the simulated 2D (poloidal/toroidal) map for Re($E_{//RF}$) in a radial plane $x = 5$ mm in front of the antenna, in scenario 2 short, toroidal phasing [0 0 π π]. Intense near field patterns are visible in front of each strap box, with a sign corresponding to the phasing. Original fields, calculated for 1 V at strap feeders, were subsequently renormalized to the nominal 20 MW coupled RF power. The RF power coupled with 1 V at the feeders is displayed as $P_0$ in Table 1. Best RF coupling was obtained with long SOLs due to voltage stand-off limits, while the antenna may not be able to deliver the full 20 MW with short SOLs. RF coupling also depends on the launched $k_{//}$ spectrum, i.e., phasing, so that $P_0$ varies according to the rule [0 0 π π] > [0 π π 0] > [0 π 0 π].

The (complex) $E_{//RF}$ field was integrated over the entire field map along tilted straight magnetic field lines (see Fig. 2). Pitch angle was 15° on scenario 2 and 9° on scenario 4. To each open flux tube, labelled in 2D by its intersection point $(x,y)$ with the poloidal cross-section $z = 0$, can be associated a complex RF potential $V_{RF}(x,y) = \int_L \mathbf{E}_{//RF}\mathbf{dl}$. Near antenna mouth, and for 1 V at the feeders, the amplitude $|V_{RF}|$ was found weakly dependant on the plasma scenario. When rescaled to 20 MW coupled $|V_{RF}| \alpha P_0{}^{-1/2}$, i.e., it is higher for short SOLs. Fig. 3 plots $|V_{RF}|$ at antenna mouth versus altitude $y$ for scenario 2 long and three phasings. $|V_{RF}|$ is non-zero on fields lines crossing the antenna aperture in the metallic wall (see Fig. 2). The poloidal profiles reveal series of peaks, whose location depends mainly on phasing, and slightly on pitch angle. The flux tubes associated to the peaks in [0 0 π π] phasing are drawn over Fig. 2. The peak topology remains to be interpreted. On simpler strap arrays, peaks were also observed and correlated with flows of parallel RF currents over the antenna front face [15]. The radial decay of $|V_{RF}|$ is governed by the evanescence of the Slow Wave in the SOL plasma. The e-fold decay lengths for $|V_{RF}|$, displayed as $L_{RF}$ in Table 1, are consistent with the skin depth $c/\omega_{pe}$ near antenna mouth: RF field penetration is deeper for short SOLs, and never exceeds 35 mm.

2D maps $V_{RF}(x,y)$ served as a driving term in SEM sheath rectification module [10] to produce 2D maps of DC potential $V_{DC}(x,y)$. Maximum DC potentials over the 2D map were recorded near the antenna mouth. Their values, displayed as $V_{DCmax}$ on Table 1, are of order $|V_{RF}|/2$, whereas $\sim|V_{RF}|/3$ is expected from independent flux tube models (e.g., [6]). $V_{DCmax}$ reaches 5.2 kV for 20 MW coupled. Higher DC potentials are observed for short SOLs than for long SOLs, due to poorer RF coupling. $V_{DC}$ maps exhibit poloidal peaks similar to Fig 3. With independent flux tube models, $|V_{RF}|$ and $V_{DC}$ would exhibit comparable radial decays. Here, nearby flux tubes were coupled, and due to the 'flute' assumption in the SEM model [10], the coupling coefficient was proportional to the length $L_{//}$ of open field lines. As $L_{//}$ was increased above some threshold, the e-fold decay lengths for $V_{DC}$ (displayed as $L_{DC}$ in Table 1) progressively became higher than $L_{RF}$. As DC potentials could penetrate further inside the discharge, spurious edge power losses significantly grew with increasing $L_{//}$. Yet the 'flute' assumption might fail for large $L_{//}$ (20 m in scenario 2, 35 m in scenario 4). Values in Table 1, corresponding to full radial broadening of $V_{DC}$, could therefore represent over-pessimistic upper bounds.

## 4. RF-induced density convection and heat loads

RF-induced localized inhomogeneous density modifications are suspected around powered ICRF launchers [3,16]. These changes were estimated in code CELLS [3]. The steady-state 2D density

**Table 1**
Summary of quantitative simulation results.

| Scenario | 2, long SOL | | | 4, long SOL | | | 2, short SOL | | | 4, short SOL | | |
|---|---|---|---|---|---|---|---|---|---|---|---|---|
| Phasing | 0 0 π π | 0 π π 0 | 0 π 0 π | 0 0 π π | 0 π π 0 | 0 π 0 π | 0 0 π π | 0 π π 0 | 0 π 0 π | 0 0 π π | 0 π π 0 | 0 π 0 π |
| $T_e$; $T_i$ (eV) | 11.7; 21.6 | | | 23; 59 | | | 11.7; 21.6 | | | 23; 59 | | |
| $v_{SOL}$(m/s) | 93 | | | 95 | | | 28 | | | 29 | | |
| $n_{ant}$ ($m^{-3}$) | $1.1 \times 10^{18}$ | | | $6.0 \times 10^{17}$ | | | $5.2 \times 10^{15}$ | | | $3.9 \times 10^{15}$ | | |
| $P_0$ mW/$V^2$ | 29.3 | 20.7 | 11.5 | 9.44 | 6.77 | 4.67 | 8.97 | 6.97 | 4.85 | 5.41 | 4.47 | 3.6 |
| $L_{RF}$ (mm) | 4.1 | 4.1 | 4.1 | 5.6 | 5.6 | 5.6 | 33 | 33 | 33 | 35 | 35 | 35 |
| $L_{DC}$ (mm) | 39 | 37 | 33 | 42 | 36 | 39 | 50 | 41 | 44 | 54 | 42 | 49 |
| $V_{DCmax}$ (kV) | 2.0 | 1.8 | 2.2 | 2.6 | 2.6 | 4.6 | 4.3 | 2.1 | 2.6 | 3.5 | 3.4 | 5.2 |
| $Q_{//max}$ (MW/$m^2$) | 8.1 | 7.4 | 8.9 | 8.9 | 9.0 | 16.0 | 3.2 | 0.9 | 2.9 | 3.2 | 1.7 | 3.5 |
| $P_{//0}$ (MW) | 1.01 | | | 1.23 | | | 1.03 | | | 1.10 | | |
| $P_{//1}$ (MW) | 2.18 | 2.21 | 2.13 | 2.48 | 2.11 | 3.04 | 1.97 | 1.24 | 1.65 | 1.98 | 1.45 | 1.95 |
| $P_{//2}$ (MW) | 1.42 | 1.60 | 1.60 | 1.82 | 1.62 | 1.83 | 1.07 | 1.01 | 1.11 | 1.05 | 1.09 | 1.03 |
| $\Delta P_{sh}$ (kW) | 403 | 579 | 582 | 587 | 392 | **597** | 40 | −17 ! | 84 | −50 ! | −6 ! | −**61 !** |

Bold values highlight the extremal results obtained over the 12 scenarios considered.

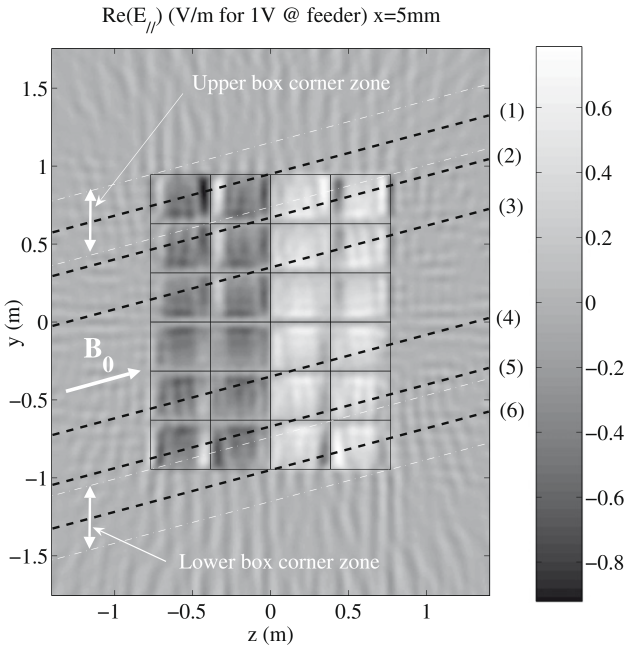

**Fig. 2.** 2D (toroidal/poloidal) map of Re($E_{//RF}$) 5 mm in front of antennna aperture, for senario 2 short, phasing [$00\pi\pi$]. Superimposed: sketch of ITER antenna structure; selected field lines and locations of upper and lower box corner zones.

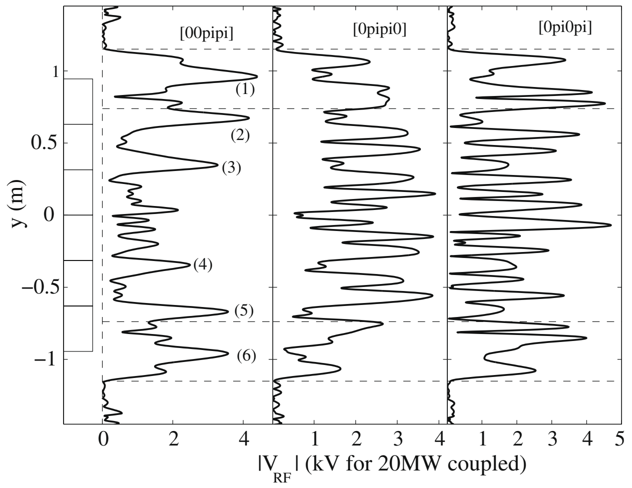

**Fig. 3.** Profiles of $|V_{RF}|$ at antenna mouth, for scenario 2 long and 3 phasings, versus altitude $y$ with respect to antenna mid-plane. Superimposed: vertical cut through ITER antenna structure; list of peaks, corresponding to the field lines numbered on Fig. 2; horizontal dashed lines: limits of upper and lower box corner zones.

balance accounts for parallel losses, the radial convective flux $nv_{sol}$, DC $E \times B_0$ transport in the gradient of the DC potential $V_{DC}(x,y)$ as well as a residual cross-field diffusivity $D_\perp = 0.04$ m$^2$/s. Neither atomic physics nor recycling was included however. Fig. 4 shows that $E \times B_0$ drifts make the density poloidally inhomogeneous. In regions where convection dominates, iso-density curves nearly align with iso-potential lines [3]. The poloidal peak structure of Fig. 3 is therefore recovered, with a radial penetration up to 10 cm. Convection tends to deplete the zones of high potential at the centre of the convective cells, all the more easily since the background particle diffusion was nearly suppressed and $v_{SOL} < 0.01\, v_{E\times B0}$ ($\sim V_{DCmax}/(B_0 L_{DC}) > 10$ km/s). The quantitative amount of depletion is sensitive to $v_{SOL}$ and $D_\perp$ which are poorly known. Over-density is observed on thin stripes above the major convective cells.

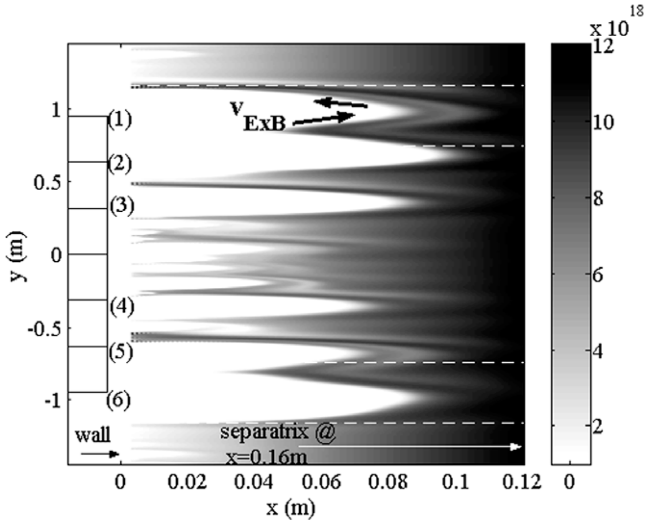

**Fig. 4.** 2D (radial/vertical) density map (unit: m$^{-3}$) for scenario 2 long, [$00\pi\pi$] phasing. $x$ is the radial distance to the first wall. Superimposed: vertical cut through ITER antenna structure; list of peaks, numbered as in Fig. 3; horizontal dashed lines: limits of upper and lower box corner zones.

Parallel heat flux densities were estimated from $Q_{//}(x,y) = 0.5en(x,y)c_s\ V_{DC}(x,y)$. Within the sound speed $c_s \alpha (T_e + T_i)^{1/2}$, the 2D map $Q_{//}(x,y)$ is the product of density $n(x,y)$ by DC potential $V_{DC}(x,y)$. Typical maps for long SOL scenarios are shown in Fig. 5. Localized peaks are observed above $Q_{//} = 8$ MW/m$^2$, i.e., well above typical local fluxes without RF. Their poloidal location was determined in Fig. 3. Significant heat fluxes are found in the first 5 cm in front of the antenna, a radial extension determined by the penetration of $V_{DC}$. For short SOL scenarios, heat flux maps look quite different from Fig. 5: highest fluxes are found near the separatrix and are present even without RF waves. Near the antenna high $V_{DC}$ peaks correspond to zones of low density and cause minor heat loads.

Table 1 sums the edge power fluxes $Q_{//}(x,y)$ over the 2D simulation domain. $P_{//0}$ stands for power losses without RF. $P_{//0} \alpha n_e T_e^{3/2}$ and is therefore important on dense and hot plasmas. $P_{//1}$ evaluates losses with rectified DC sheath potentials and unperturbed density distribution, for 20 MW coupled. As $V_{DC}$ increases in presence of RF power, $P_{//1} > P_{//0}$. $P_{//2}$ was estimated in presence of rectified DC potentials and RF-induced density transport. $E \times B_0$ convection tends to deplete the zones of high $V_{DC}$, so that $P_{//2} < P_{//1}$. Two classes of scenarios emerge from Table 1, depending on local density. On short SOL profiles the power losses $\Delta P_{sh} = P_{//2} - P_{//0}$ attributed to RF sheaths are found small compared to $P_{//0}$. This arises because $V_{DC}$ is only high in regions of low density. In several cases $\Delta P_{sh}$ becomes negative: the density depletion over-compensates the increase of DC potential. In long SOL cases, high density penetrates up to the antenna mouth, and the estimated $\Delta P_{sh}$ are typically 400–600 kW (i.e., 2–3% of 20 MW coupled) with full radial broadening. $\Delta P_{sh}$ is lost over a small surface of $\sim$0.16 m$^2$.

## 5. Discussion and outlook

In this paper a simple RF sheath model was applied to open field lines in front of the ITER ICRF antenna to estimate parallel heat fluxes. Localized maximal sheath voltages, 2–5 kV, appear higher than those measured on present machines, e.g. in [17], and could lead to unipolar arcing and fast localized erosion of the PFC material. As observed experimentally [4] quantitative results strongly depend on the local density, so that measurements on existing devices probably need to be extrapolated to ITER power levels and RF coupling conditions in order to allow fair comparison. Besides

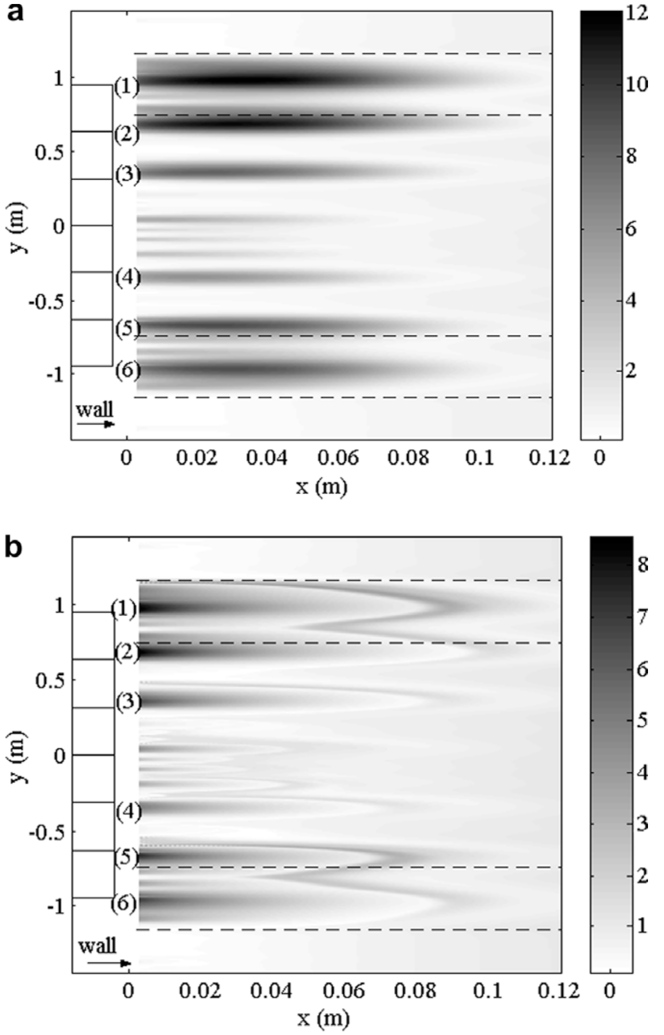

**Fig. 5.** 2D (radial/poloidal) maps of parallel heat fluxes (unit MW/m$^2$) for scenario 2 long, [0 0 π π] phasing. Superimposed: vertical cut through ITER antenna structure; list of peaks, numbered as in Fig. 3; horizontal dashed lines: limits of upper and lower box corner zones. Calculation with (a) unperturbed and (b) perturbed density distributions.

present day measurements might lack the spatial resolution to catch localized maximal potentials. Heat fluxes are only substantial for long SOLs, where large DC potentials and high density are found simultaneously on the same flux tubes. Therefore ICRF antenna operation on ITER might result from a trade-off between RF coupling constraints and tolerable heat fluxes.

Within our sheath model, qualitative insight was gained on the 2D topology of power fluxes around the ITER antenna. Heat loads are highly localized in poloidal peaks whose distribution is mainly determined by the toroidal strap phasing. Peaks extend radially where DC potentials can penetrate, i.e. a few centimetres with the density profiles used. Above some threshold in connexion length $L_{//}$, coupling flux tubes by exchange of transverse RF currents enhances this radial penetration. $Q_{//}$ at the antenna mouth is weakly affected, but the total amount of spurious power losses increases. RF-induced $E \times B_0$ convection expels density from zones of high potential and decreases the heat fluxes locally.

Quantitative estimates should be considered as orders of magnitude. Uncertainty remains at each step of the modelling. Several improvement could be envisaged:

- Density and temperature profiles are poorly constrained in the far SOL. The density range at the antenna mouth presently covers two orders of magnitude.
- RF field propagation was evaluated in absence of RF sheaths. Near field patterns depend on details of the antenna front face design, in particular its grounding scheme.
- Several RF-sheath models exist in the literature, whose validation remains sparse. Here, radial broadening of $V_{DC}$ was identified and should be studied more carefully, to understand its mechanisms and relevant parameters. On long field lines the predicted broadening is high enough to be measured in present magnetic fusion devices, but was not yet confronted to experiments. Full broadening of DC potentials was retained here because it is a pessimistic assumption for edge power losses. It might however be over-pessimistic on long open field lines.

## Acknowledgements

This work, supported by the European Communities under the contract of Association between EURATOM and CEA, was carried out within the framework of the contract EFDA 07/1700-1572. The views and opinions expressed herein do not necessarily reflect those of the European Commission.

## References

[1] C.E. Thomas et al., JNM 220–222 (1995) 531.
[2] T. Imai, H. Sawada, Y. Uesugi, S. Takamura, JNM 266–269 (1999) 969.
[3] M. Bécoulet et al., Phys. Plasma 9 (6) (2002) 2619.
[4] L. Colas et al., Nucl. Fus. 46 (2006) S500.
[5] K. Saito et al., J. Nucl. Mater. 363–365 (2007) 1323.
[6] F.W. Perkins, Nucl. Fus. 29 (4) (1989) 583.
[7] D.A. D'Ippolito, J.R. Myra, et al., Nucl. Fus. 38 (1998) 1543.
[8] V. Lancellotti et al., Nucl. Fus. 46 (2006) S476.
[9] M. Brambilla, Plasma Phys. Control. Fus. 31 (5) (1989) 123.
[10] E. Faudot et al., Phys. Plasmas 13 (2006) 042512.
[11] D.A. D'Ippolito et al., Phys. Fluids B5 (10) (1993) 3603.
[12] A. Loarte et al., In: Proceedings of the Twenty second IAEA Fusion Energy Conference – 50th Anniversary of Controlled Nuclear Fusion, IT/P6-13.
[13] R. Schneider, X. Bonnin, et al., Contrib. Plasma Phys. 46 (2006) 3.
[14] B. Lipschultz et al., Nucl. Fus. 47 (9) (2007) 1189.
[15] L. Colas et al., Nucl. Fus. 45 (2005) 767.
[16] L. Colas et al., Plasma Phys. Control. Fus. 49 (2007) B35.
[17] B. Lipschultz et al., Nucl. Fus. 41 (2001) 585.